# Automated detection of volcanic seismicity using network covariance and image processing

Sean P. Maher

U.S. Geological Survey, California Volcano Observatory, Moffett Field, California, USA; now at Zanskar Geothermal & Minerals, Inc., Salt Lake City, Utah, USA

Phillip B. Dawson

U.S. Geological Survey, California Volcano Observatory, Moffett Field, California, USA

Alicia J. Hotovec-Ellis

U.S. Geological Survey, California Volcano Observatory, Moffett Field, California, USA

Weston A. Thelen

U.S. Geological Survey, Cascades Volcano Observatory, Vancouver, Washington, USA

Robin S. Matoza

Department of Earth Science and Earth Research Institute, University of California Santa Barbara, CA, USA

**Citation:** Maher, S.P., P.B. Dawson, A.J. Hotovec-Ellis, W.A. Thelen, and R.S. Matoza (2024), Automated detection of volcanic seismicity using network covariance and image processing, *Seismol. Res. Lett.*, doi:10.1785/0220240014

#### Abstract

Seismicity at restless volcanoes commonly features a variety of signal types reflecting both volcano-tectonic and fluid-driven source processes. However, traditional catalogs of seismicity are often incomplete, especially with respect to events with emergent onsets such as those driven by the dynamics of magmatic and hydrothermal fluids. The detection of all discrete events and continuous seismic tremor, regardless of the underlying source processes, would therefore improve the ability of monitoring agencies to forecast eruptions and mitigate their associated hazards. We present a workflow for generalized detection of seismic events based on the network covariance matrix (Seydoux et al., 2016). Our contributions enable the method to simultaneously detect continuous and short-duration (< ~10 s) events, provide information about the frequency content of the signals, and to refine the initial detection times by an order of magnitude (from window lengths of 75 to 7.5 s). We test the workflow on a 15-month record of seismicity with 23 stations at Mammoth Mountain, California (7/2012-10/2013) and detect 62% of long-period events and 94% of volcano-tectonic events in the existing Northern California Earthquake Data Center catalog. In addition, ~3000 events not included in the catalog and thousands of tremor signals are found. The method is suitable for near-real time analysis of continuous waveforms and can provide a valuable supplement to existing algorithms to improve the completeness of catalogs used for monitoring volcanoes.

## Introduction

A fundamental task of volcano observatories is to monitor the rates and types of earthquakes near volcanoes, since magmatic unrest is almost always accompanied by changes in seismic activity (McNutt, 1996; Thompson, 2015). Timely detection of volcanic seismicity is therefore essential for forecasting eruptions and mitigating their hazards. Of particular interest are the types of earthquakes broadly classified as long period (LP) seismicity, including tremor and discrete LP events, whose potential source mechanisms have been attributed more directly to magmatic fluids than volcano-tectonic (VT) earthquakes (Chouet, 1996; Chouet & Matoza, 2013). In contrast to VT seismicity, LP seismicity typically exhibits lower frequency content, lack of identifiable phases, and emergent onsets. LP seismicity can provide valuable insights into the behavior of magmatic fluids, but it is often undetected by existing algorithms for routine operational monitoring such as network-coincident triggers based on the short-time-average/long-time-average (STA/LTA) of individual waveforms. These methods require abrupt changes in amplitude, making them well-suited for tectonic and VT events but less sensitive to signal types with emergent onsets, such as LP events and tremor. Therefore, new practical approaches are needed to improve near-real-time detection of LP seismicity and enhance the capabilities of volcano observatories.

Traditional methods for volcano seismic detection rely on a combination of amplitude-based single-station triggering, phase association, and manual data review (McNutt et al., 2015; Thompson, 2015). For example, tectonic and VT events at California's volcanoes are automatically detected by STA/LTA triggering performed by the Northern California Earthquake Data Center (NCEDC), while LP events are manually identified and labeled by an analyst at the U.S. Geological Survey California Volcano Observatory (CalVO) (Pitt et al., 2002; Pitt & Hill, 1994). LP events that are detected by the automatic system require an analyst to review the event and subjectively change the event label to LP. This approach suffices for the detection of VT signals with abrupt amplitude changes and well-separated phase arrivals but suffers from a reliance on subjective and resource-limited analyst labor when applied to the detection of events that don't fit a volcano-tectonic description.

There are many emerging methods that now employ supervised machine learning algorithms to detect tectonic seismicity (Malfante et al., 2018, and references therein). Machine learning algorithms trained on representative samples of signal types can perform exceptionally well for both VTs and LPs (Beyreuther et al., 2008; Ciaramella et al., 2011; Cortés et al., 2021; Reynen & Audet, 2017; Titos et al., 2019). However, supervised machine learning models require large, labeled datasets, which are often not available for LP seismicity in volcanic settings. Additionally, models trained at one volcano may not perform well in other study areas with different seismic characteristics, although transfer learning approaches are being developed to mitigate this problem (Bueno et al., 2020; Titos et al., 2020).

Barring significant advancements in the generalization of machine learning methods and availability of labeled datasets, unsupervised methods based on simple mathematics remain attractive. Several alternatives to traditional methods and supervised machine learning targeted toward LP seismicity have been explored. Single-station alternatives to amplitude triggering utilize different aspects of seismic data, such as kurtosis of the waveform (Langet et al., 2014) or statistical moments of the power spectrum (Galluzzo et al., 2020), but these may still be sensitive to local noise variations. Unsupervised machine learning methods use variations on clustering algorithms to group signals based on similarity measures (Messina & Langer, 2011; Seydoux et al., 2020; Yoon et al., 2015), but these methods may require large datasets for comparison and may not detect previously unseen or infrequently occurring signal types. Multi-station methods, such

as eigenvalue decomposition of the network covariance matrix (Seydoux et al., 2016), offer mathematically simple representations of coherence across a seismic network, suppressing local noise sources and requiring little data or *a priori* knowledge.

In this study we test the applicability of an automated network covariance-based approach to volcano seismic event detection (Seydoux et al., 2016; Shapiro et al., 2023) and propose new functionality to improve its effectiveness. Compared to traditional methods, network covariance offers improved detection of LP signals, and unlike machine learning methods it requires no model building, data labeling, or *a priori* knowledge about the seismicity. Our contribution includes new techniques for data pre-processing, noise reduction, dynamic thresholding, quality control, and signal classification. Using vertical component seismic data from Mammoth Mountain, California, as an example, we compare results to the existing catalog used for monitoring by CalVO. We show how this tool can be used to supplement the existing monitoring algorithms and improve detection of LP events.

#### **Mammoth Mountain Dataset**

While the detection method we propose is generally applicable to any seismic network, we focus on data from Mammoth Mountain, California. This volcanic complex consists of 25–30 overlapping dacitic domes and peripheral mafic vents over a ~5 km diameter area on the southwestern boundary of the Long Valley Caldera (blue outline in

Figure 1). Formation of the edifice stopped ~50 ka, and the most recent eruption in the area occurred ~8.5 ka at Red Cones (Hildreth & Fierstein, 2016). Ongoing migration of magmatic fluids beneath the volcano is indicated by multiple swarms of VT and LP events in recent history (Hill et al., 1990; Hill & Prejean, 2005; Lin, 2013; Shelly et al., 2015; Shelly & Hill, 2011) and by elevated CO<sub>2</sub> emissions leading to tree kill zones and human fatalities (Lewicki et al., 2014, 2019; Peiffer et al., 2018; Sorey et al., 1998). A mid-crust annulus of fluid-transport pathways surrounding a potentially magma-bearing core has been imaged in high-precision earthquake locations (Hotovec-Ellis et al., 2018; Prejean et al., 2003). Mammoth Mountain is consequently one of the best-instrumented volcanoes in California, with 12 telemetered seismic stations (6 broadband and 6 short period) located within 8 km of the summit.

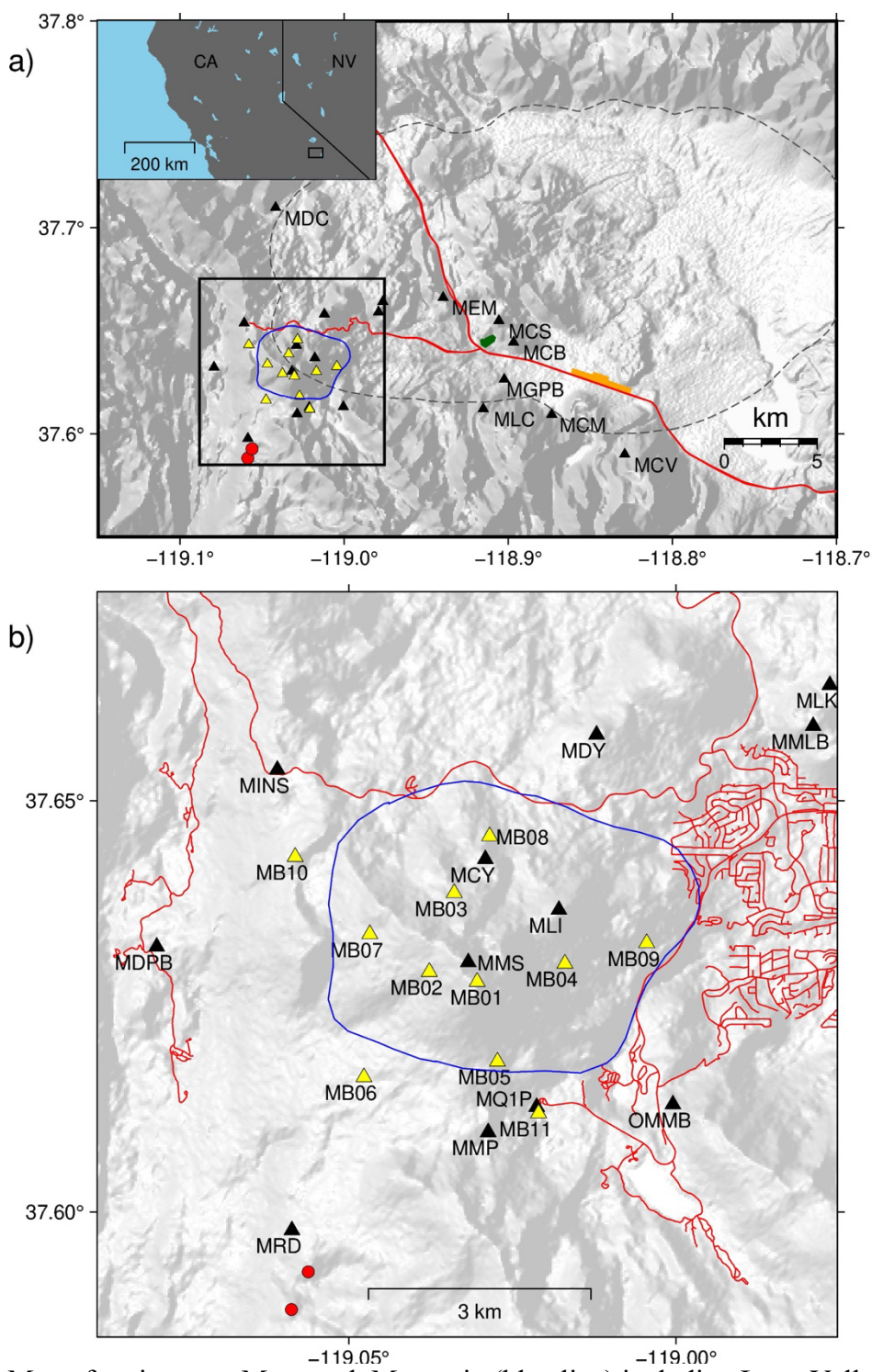


Figure 1. a) Map of region near Mammoth Mountain (blue line) including Long Valley Caldera (dashed gray line). Major roads are shown as red lines, a geothermal power plant is shown in green, and an airport is shown in orange. Triangles represent seismometers in the permanent network (black) and temporary deployment (yellow). Red circles show the location of Red Cones. Black square shows the bounds for

Figure 1b. Inset shows location of the map area (black box) in the context of California (CA) and Nevada (NV). b) Search area for local earthquakes. Red lines show roads serving the ski resort and the town of Mammoth Lakes. Topography data are SRTM15+V2.5.5 (Tozer et al. 2019).

We focus on the time period from 07/2012 to 10/2013, when the permanent seismic network was supplemented with 11 broadband stations (Dawson et al., 2016; Dawson & Chouet, 2019). During this period swarms of VT and LP events occurred, providing targets for testing the detection capability of our workflow. The NCEDC catalog lists 191 LPs and 1747 VTs in our study area during this period. This study period spans all seasons, allowing for assessment of detection performance during variable noise conditions. The mountain and nearby town of Mammoth Lakes are year-round destinations for resort skiing and mountain biking, with a resident population of ~7,000. Potential cultural sources of seismic noise include ski lifts, avalanche blasting, pumping of water and sewage, vehicle traffic, aviation, and geothermal power plant operations. Natural sources of surface noise such as avalanches and rockslides may also be present in the data.

# **Detection Workflow**

# Network covariance and spectral width

Our detection approach is based on the eigenvalue decomposition of the network covariance matrix, as introduced in the context of volcanic seismicity by Seydoux et al. (2016) and recently reviewed by Shapiro et al. (2023). The method emphasizes coherence of seismic energy across a network, enabling detection of signals with emergent onsets and suppressing local noise sources that may be spuriously triggered by single-station methods such as STA/LTA thresholding or pattern matching on spectrograms. The network covariance matrix C(f) is formed by the average cross-spectra between all station pairs over a group of M overlapping windows:

$$\mathbf{C}(f) = \frac{1}{M} \sum_{m=1}^{M} \mathbf{u}_m(f) \mathbf{u}_m^{\dagger}(f), \tag{1}$$

where  $u_m(f)$  is a column vector of complex Fourier spectra for waveforms at each station in the subwindow number m, and  $\dagger$  denotes a complex conjugate. The Fourier spectra are estimated in windows with duration  $\delta t$  and overlap ratio r, giving a duration for the covariance window of  $\Delta t = Mr\delta t$ . The covariance matrix is thus a 4D array (time, frequency, stations, stations).

In practice, the dimensionality of C(f) can be reduced by considering the distribution of its eigenvalues  $(\lambda_i)$ . When sorted in decreasing order, the distribution of  $\lambda_i$  is strongly peaked at the first eigenvector for a time-frequency pixel representing a coherent wavefield dominated by a single source. If the distribution of  $\lambda_i$  is broad and gradually decreasing an incoherent wavefield arising from many independent sources is implied (Seydoux et al., 2016). The broadness of the distribution, defined as the spectral width  $(\sigma)$ , therefore provides a proxy for the number of sources in the wavefield, with lower values indicating fewer sources:

$$\sigma = \frac{\sum_{i=1}^{N} (i-1)\lambda_i(f)}{\sum_{i=1}^{N} \lambda_i(f)},$$
(2)

where N is the matrix rank and is here equivalent to the number of stations. Plotting  $\sigma$  as a function of time and frequency yields a spectrogram-like image that can be interpreted as a measure of coherence across a seismic network, rather than spectral power at an individual station.

While the spectral width technique indicates the approximate timing and frequency content of coherent signals, it does not provide a method for systematic extraction of that information. Previous studies have identified specific signals of interest through manual processing of  $\sigma$  (Soubestre et al., 2021), setting thresholds on the average  $\sigma$  in hand-picked frequency bands (Seydoux et al., 2016), thresholding the ratios of  $\sigma$  between different frequency bands (Maher et al., 2023), or template matching on stacked  $\sigma$  spectra from known events (Permana et al., 2022). Here, we aim to develop a new practical workflow based on image processing to automatically detect seismicity from the  $\sigma$  matrix.

# Workflow overview

An overview of our proposed workflow is shown in Figure 2, and individual steps are discussed in the following sections. To suppress local noise and background variations we first pre-process the raw seismogram data. We then make detections from the  $\sigma$  matrix using image processing techniques. To improve the time resolution of detections for short-duration events, we employ a second detection step using the summed covariance. To avoid analysis of known events, we then compare detection times with a standard catalog. To further mitigate dubious detections and teleseismic surface waves, we screen detections using waveform cross-correlation and detection quality estimates. Finally, we assign remaining events a label of VT or LP based on the frequency content of the  $\sigma$  detection.

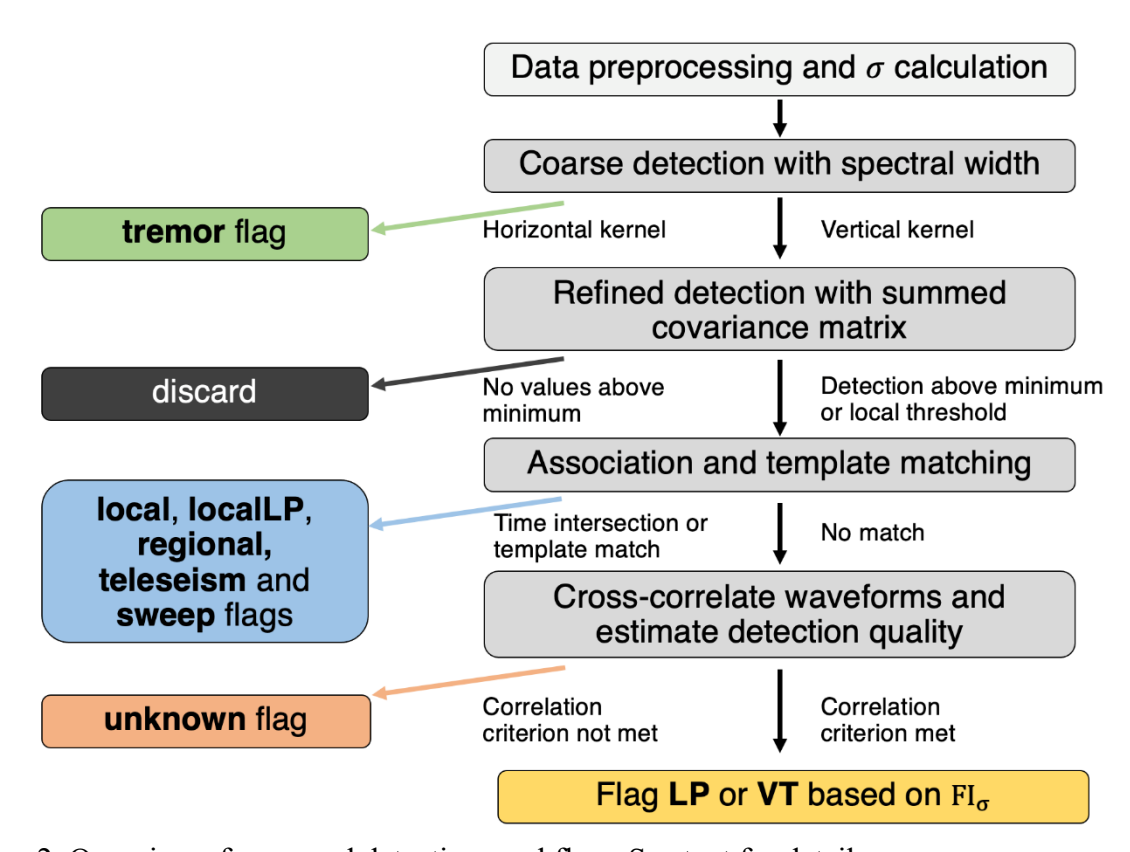


Figure 2. Overview of proposed detection workflow. See text for details.

## Pre-processing and spectral width calculation

To suppress unwanted artifacts in spectral width arising from zero-filled data gaps (Figure 3a) we first fill gaps with artificial white noise (Figure 3b). The white noise consists of random numbers sampled from a Gaussian distribution with mean and standard deviation equal to that of the available data for that station on that day. Filling gaps with white noise rather than removing stations ensures consistent background values of  $\sigma$  through time and allows detection of events during gaps at individual stations. Before gap filling, individual trace segments are detrended with a linear least-squares fit; after gap filling, the waveforms are detrended by subtraction of the mean. The waveforms are then low-pass filtered at 25 Hz, and the sample rate is decimated from 100 to 25 Hz to reduce computation time. After decimation, instrument responses are removed to ensure consistent responses across different instrument types. Pre-filtering with corner frequencies at 0.005, 0.01, 10 and 12 Hz is used in the instrument response removal. One-bit spectral pre-whitening is then applied to the waveforms as in previous studies (e.g., Journeau et al., 2020; Seydoux et al., 2016; Soubestre et al., 2019) to eliminate the effect of signal amplitudes and emphasize phase coherence across the network.

We then calculate the network covariance and spectral width using  $\delta t = 15$  s, r = 0.5 and M = 20. This  $\delta t$  is relatively short in comparison to previous studies which were focused on continuous tremor; however it still allows time for seismic waves to propagate across the ~10 km aperture of the network. For example, Seydoux et al. (2016) and Journeau et al. (2022) used  $\delta t = 48$  s while Soubestre et al. (2018) used  $\delta t = 1,000$  s. Shorter windows allow us to have better time resolution for short-duration LP and VT events, but they reduce frequency resolution at lower frequencies. Since we are mainly interested here in short-duration LP and VT events at Mammoth Mountain, we limit our analyses to the frequency band 1–10 Hz. We note that our M value is approximately equal to the number of stations in the network, as recommended for a statistically robust estimation of the covariance matrix (Seydoux et al., 2016).

After calculating the network covariance matrix and spectral width, we further process  $\sigma$  with a noise-reducing spectral gating technique adapted from Sainburg et al. (2020). This procedure creates a mask over the  $\sigma$  matrix and increases the value of pixels above a threshold set by the mean and standard deviation of a manually defined quiet window of  $\sigma$ . The effect of this masking is to suppress minor background variations and improve visibility of the coherent signals (Figure 3c).

#### Coarse detection with spectral width

To make automatic detections from the spectral width matrix without averaging in user-defined frequency bands, we use smoothing and thresholding techniques from image processing (e.g., Dey, 2018). We separately convolve the noise-reduced spectral width matrices with a frequency kernel (100x1 pixels, or 3.34 Hz) and a time kernel (1x100 pixels, or 748 seconds) to created blurred matrices for detection of short-duration and continuous signals, respectively (Figure 3e,g). Compared to a single convolution operation with a 100x100 kernel, this approach allows independent detection of overlapping tremor and impulsive events. The effect of the kernels is to blur together pixels in the same detection even if some of the values approach the level of the background; the choice of kernel sizes depends on the sampling rate, bandwidth of interest, and time resolution in the spectral width matrix.

The blurred matrices are thresholded based on a 4-hour moving average minus the standard deviations and multiplied by a factor of -2 for the frequency kernel and -4 for the time kernel. These factors were manually chosen through trial and error; a higher threshold is set for the time kernel to avoid duplicate detection of closely spaced short-duration events.

Connected pixels that pass the thresholds are grouped into detections, and detections with size < 20 pixels are excluded. Small groups (< 20 pixels) likely correspond to background variations and so are excluded as false positives; however, some small groups may represent weaker or less coherent signals. Finally, we fill gaps between disconnected frequency segments with overlapping start/stop times if the frequency separation is < 2 Hz, and between disconnected time segments with overlapping frequency bounds if the time separation is < 60 minutes. Examples of detections made with this method are shown in Figure 3d. Detections made with the time kernel are flagged as "tremor" (e.g., Figure S1) and put aside, while detections made with the frequency kernel are further processed with the steps described below.

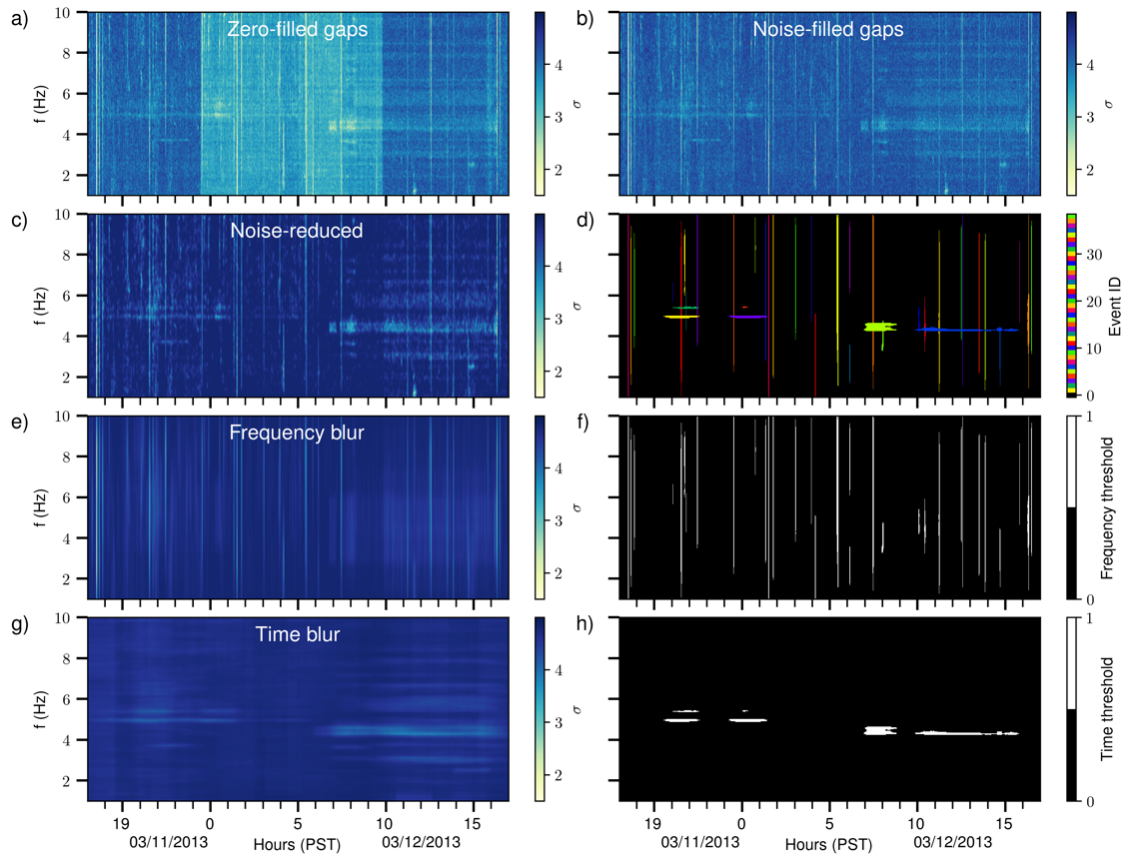


Figure 3. Example of pre-processing and coarse event detection with the spectral width matrix  $(\sigma)$ . a) Spectral width matrix for a day of data at Mammoth Mountain. Data gaps at 9 out of 23 stations are filled with a default value of zero, causing artificial reduction in spectral width. b) Spectral width matrix for the same day after filling data gaps with white noise. c) Spectral width after filling gaps with white noise and using spectral gating to suppress background variations. d) Independent detections shown with different colors after thresholding and post-processing. e) Noise-reduced spectral width after frequency blurring. f) Detection of short-duration events by thresholding of frequency-blurred spectral width. g) Noise-reduced spectral width after time blurring. h) Tremor event detection by thresholding of time-blurred spectral width.

# Refined detection with summed covariance matrix

Detections made with the frequency kernel provide an approximate time of seismic events, but refined times are desirable because the signals from local events are short in duration ( $\sim$ 5–10 s) relative to the  $\sigma$  window length (75 s in this study). Multiple local events may occur in a single  $\sigma$  detection window, and ambient noise in the  $\sigma$  window may alter the spectral signature of the signals themselves. We therefore propose the following time refinement approach based on the summed covariance matrix.

Before averaging together M windows to make windows with length  $\Delta t = 75$  s, our covariance matrices consist of complex Fourier cross-spectra with subwindow lengths of  $\delta t = 15$  s. As these are overlapped by r = 0.5, the finest time resolution available is effectively 7.5 s. We take the absolute value of these cross-spectra and sum across all station pairs (e.g., Figure 4c). We then apply the spectral gating technique to reduce background noise on this matrix (Figure 4d). We next convolve the noise-reduced matrix with a frequency kernel (1x100 pixels or 3.34 Hz) and threshold based on the matrix mean plus standard deviation multiplied by a factor of 2 (Figure 4e,f). If this automatic threshold falls below a manually chosen minimum of  $1.5 \times 10^5$  (a value that is primarily dependent on the number of stations used) we enforce this minimum threshold to discard weak detections. The timing and frequency bounds of any detections made in this process are recorded, providing a time-refined catalog with initial information about duration and spectral content. Examples of final detections made with this method are shown in Figure 4g.

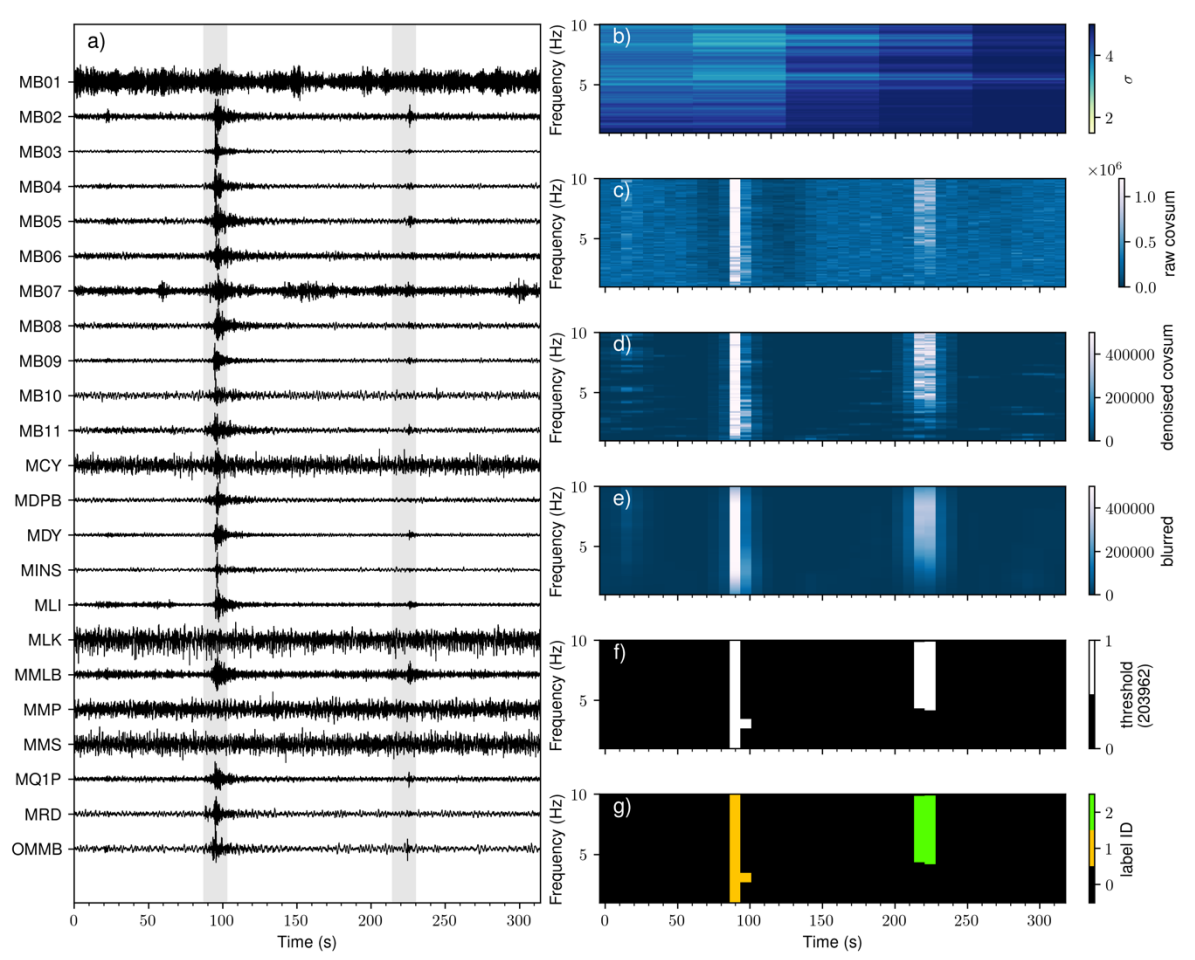


Figure 4. Example of time-refinement process for a single detection made by spectral width. a) Vertical component waveforms (bandpass-filtered 0.5–10 Hz) during the detection window (04:11:57–04:17:11 PST on 7/2/2013). Gray shaded regions show the times of separate detections made during time-refinement. b) Spectral width matrix in the detection window. c) Summed covariance matrix in the detection window. d) Noise-reduced version of the summed covariance matrix. e) Noise-reduced summed covariance after frequency-blurring. f) Blurred covariance after thresholding based on the mean and standard deviation of the window. g) Two detections made after thresholding and post-processing.

#### Association and template matching

Since seismic monitoring at Mammoth Mountain is already performed with automatic locations and analyst-based arrival-time relocation, detections made by network covariance may correspond to events detected by routine monitoring. To compare our catalog with an existing database of events, we first query the NCEDC for local events (x < 8 km, all magnitudes) and regional events (8 < x < 250 km, M > 1) and we query the Advanced National Seismic System Comprehensive Catalog (ANSS ComCat) for teleseismic events (x > 250 km, M > 4), where x is the distance from the summit of Mammoth Mountain and M is magnitude. We then predict phase arrival times at the summit of Mammoth Mountain for each event using Obspy's taup function. Since Obspy's taup function only predicts body wave travel times, we further estimate surface wave arrival times according to the epicentral distance and constant velocities of 0.5, 1, and 2 km/s. We flag spectral-

width detections as "local," "regional," or "teleseism" if its time window intersects a predicted phase arrival time from an earthquake listed in the respective catalog.

Additionally, we noticed during visual inspection of our results that the summed covariance matrices of some detections exhibit a characteristic upward- or downward-gliding feature in a narrow spectral band (Figure S2). We do not know the exact cause of this feature but assume it is a Doppler shift caused by aircraft passing over the seismic network. A small airport in the Long Valley Caldera serves commercial air travel to and from the Mammoth Mountain ski resort (

Figure 1a). To reduce the flagging of these detections as new LP or VT events, we perform image-based template matching on the summed covariance matrices using the eight manually picked templates shown in Figure S2a. Detections with a template matching coefficient greater than 0.8 are flagged as "sweep" events.

# Waveform cross-correlation and quality estimation

While the association step identifies some teleseismic events, there are remaining detections featuring highly similar waveforms across the network that resemble surface waves from regional or teleseismic earthquakes. Conversely, the waveforms of some detections show no discernable signal. These often correspond to tremor-like detections with broad enough bandwidth to be detected by the frequency kernel. To avoid flagging either of these detection types as new LP or VT events we cross-correlate the vertical component waveforms in the detection windows for all station pairs. We expect that teleseismic surface waves will have high correlation across all stations while false alarms or weak tremor-like signals will have low correlation across all stations. If > 2stations do not correlate with > 2 other stations with a correlation coefficient greater than 0.25, we flag the detection as "unknown" (e.g., Figure S3). If > 2 stations correlate with > 2 other stations with maximum coefficient greater than 0.5, we flag the detection as surface waves (e.g., Figure S4). Cross-correlations are estimated on normalized vertical component waveforms bandpassfiltered at 0.5–10 Hz in windows starting 5 seconds before the detection on-time and ending 10 seconds after the detection off-time. These window lengths can range from 22.5 seconds to several minutes in length. Addition of time on either side of the detection window is necessary because the window may not capture the full waveform for the event at every station.

This cross-correlation step also forms part of the basis of our estimate of detection quality  $(Q_d)$ . Since newly detected events may be reviewed by an analyst for phase picking and arrival-time based location, "better" detections should be prioritized for analysis. We set a threshold to exclude the lowest-quality detections from the catalog. We define detection quality as:

$$Q_d = \operatorname{mean}(C_s) + \operatorname{mean}(\sigma_d^{-1}) + \frac{N_C}{N}, \tag{3}$$

where  $C_s$  is the summed covariance matrix in the detection window normalized from 0-1,  $\sigma_d$  is the spectral width matrix in the detection window normalized from 0-1,  $N_c$  is the number of stations meeting the correlation criterion, and N is the total number of stations. Possible values of  $Q_d$  range from 0 to 3. Low-quality detections have low covariance values, high spectral width values, and few stations that meet the correlation criterion (Figure 5a) while high-quality (high  $Q_d$ ) detections have high covariance values, low spectral width values, and many stations that meet the correlation criterion (Figure 5b). Histograms of  $Q_d$  for all detections (except tremor detections) are shown in Figure S5.

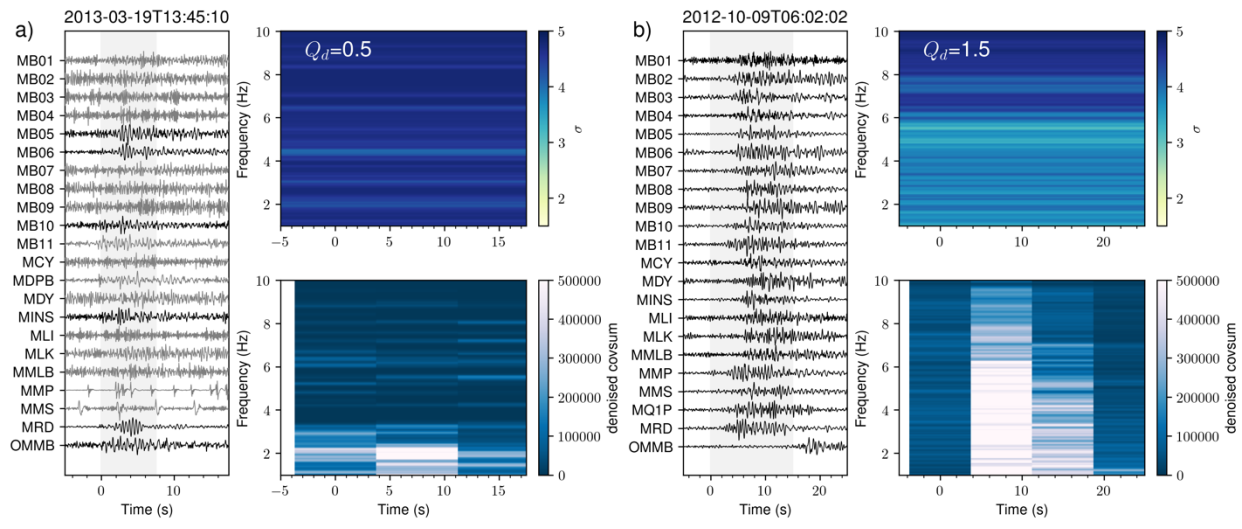


Figure 5. Examples of a low-quality LP detection (a) and a high-quality LP detection (b). The low-quality detection has only five waveforms meeting the correlation criterion (shown in black), while the high-quality detection has 22 waveforms meeting the criterion. Gray shaded regions show the time of the detection window obtained from the summed covariance matrix. Compared to the high-quality detection, the low-quality detection has higher spectral width values and lower values of summed covariance.

# Classification

We classify the remaining unflagged detections as LP or VT events according to the spectral content of the  $\sigma$  matrix in the corresponding window. We propose a classification metric similar to the widely used Frequency Index (FI), which quantifies the ratio of a signal's spectral power in a high and low frequency band (Buurman & West, 2010). Our spectral-width frequency index, FI $_{\sigma}$ , can be defined as:

$$FI_{\sigma} = \log_{10} \left( \frac{\frac{1}{size(\sigma_d)} \sum_{f_1}^{f_2} \sum_{t_1}^{t_2} \sigma_d}{\frac{1}{size(\sigma_d)} \sum_{f_3}^{f_4} \sum_{t_1}^{t_2} \sigma_d} \right), \tag{4}$$

where  $t_1$  and  $t_2$  are the respective start and end times of the  $\sigma_d$  window and  $f_1-f_4$  are manually-chosen bounds for the frequency bands. Here we choose  $f_1=1$  Hz,  $f_2=3$  Hz,  $f_3=5$  Hz, and  $f_4=8$  Hz. Detections with  $FI_{\sigma}<0$  are flagged as LP due to their greater coherence in the lower frequency band, while detections with  $FI_{\sigma}>0$  are flagged as VT. In most cases the  $FI_{\sigma}$  classification agrees with the more traditional network-median FI-based classification (Matoza et al., 2014), but our approach has the advantage in time and computation by using the previously calculated  $\sigma$  matrix. Histograms of FI and FI $_{\sigma}$  for LP and VT detections are shown in Figure S6.

# Detection and classification of seismic signals at Mammoth Mountain

Table 1 lists the number of each type of detection made by our workflow in the study period and compares with the number of catalog events where applicable. We detect 119 out of 191 local LPs (62%) and 1634 out of 1747 local VTs (94%), as well as 1110 new LPs and 4702 new VTs. Of these, imposing a quality threshold of  $Q_d > 1$  leaves 331 new LPs and 2180 new VTs. In addition,

we detect 1917 previously unknown tremor-like signals. The detection rates for known events outside the network are lower (47% for regionals and 5% for teleseisms); however, this is expected since not all distant events will be registered at the network or coherent across most stations.

Table 1. Counts of each spectral width detection type and corresponding NCEDC catalog counts.

	Spectral width	NCEDC Catalog	Percent detected
	detections	events	
Local LP	119	191	62%
Local VT	1634	1747	94%
Regional	2403	5146	47%
Teleseism	1046	22544	5%
New VT	4702		
New LP	1110		
Sweep	305		
Tremor	1917		
Unknown	1781		
Surface waves	200		

Among the known events that are missed by our method, some are masked by cultural noise, and many are simply too weak to pass the blurred covariance threshold. Figure 6 shows examples of analyst-flagged LP events that were not detected by our method. In Figure 6a, an episode of broadband and long-duration coherence (discussed later in this section) obscures any potential signal of a LP listed in the catalog. In Figure 6b and Figure 6c, faint  $\sigma$  signals associated with catalog events are too weak to pass the threshold, which is set by the local mean and standard deviation and is influenced by the surrounding stronger VT signals. In Figure 6d, six known LPs occur in a single  $\sigma$  detection window, but only the strongest four are cataloged during the time-refinement process.

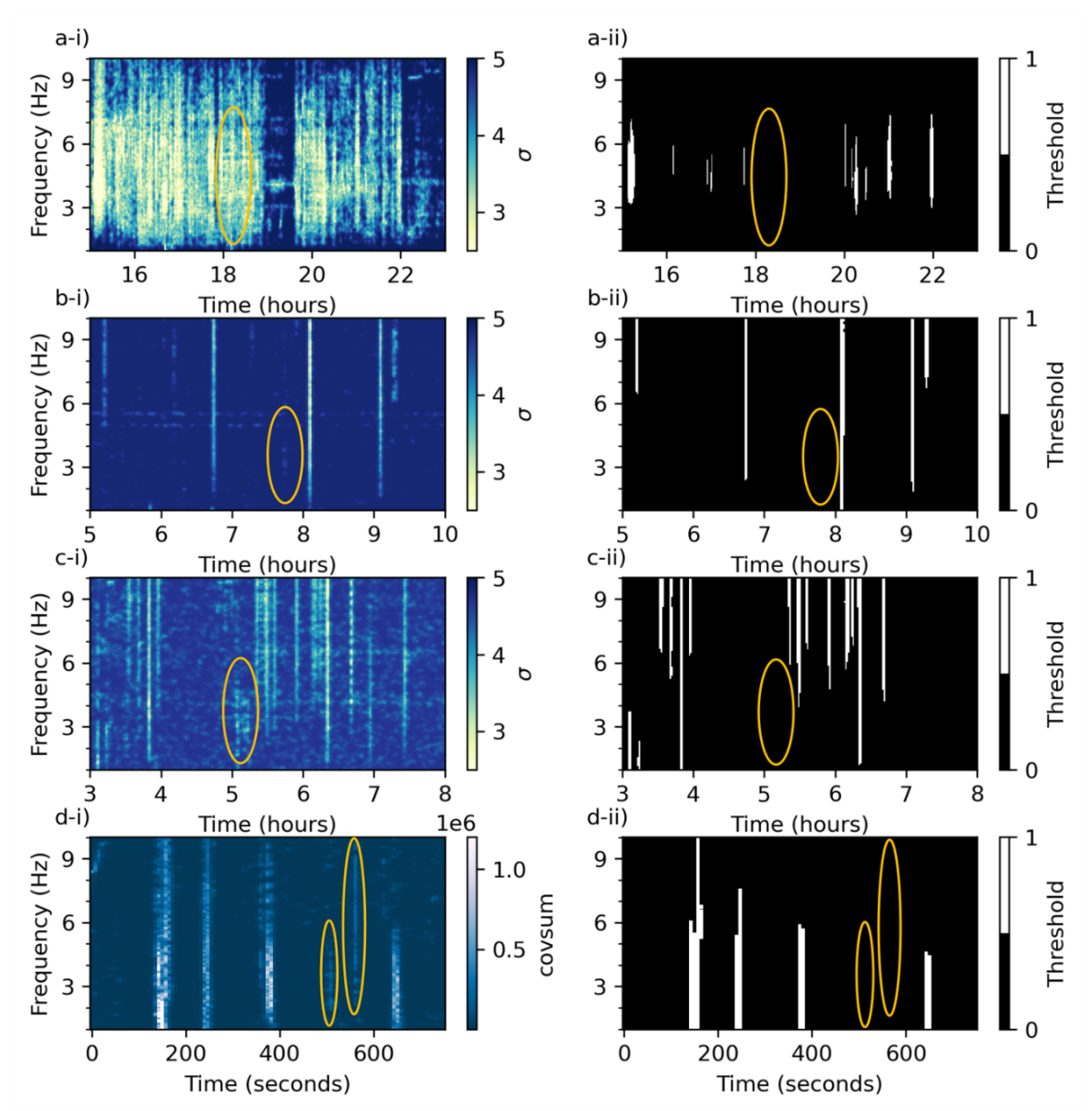


Figure 6. Examples of known long-period events that were not detected by our method. a-i) Noise-reduced spectral width for an event at 11:10:47 PST on 9/4/2012. Orange oval shows the time and expected frequency of the event, but the detection is hidden by noise. a-ii) Threshold applied to the spectral width matrix in 6a-i, showing that the known LP is missed. b-i) Noise-reduced spectral width for an event at 00:45:46 PST on 6/8/2013. The known event is barely visible and does not pass the detection threshold as shown in b-ii). c-i) Noise-reduced spectral width for an event at 22:5:14 PST on 9/21/2013. The known event is visible but does not pass the detection threshold as shown in c-ii). d-i) Summed covariance matrix for a spectral width detection at 20:50:38 PST on 8/25/2013. Six known LPs occur in this window, but two are not detected (orange ovals), as they do not pass the threshold shown in d-ii).

Figure 7a and 7b compare the weekly rates of LPs and VTs, respectively, between the two catalogs. The weekly rates are generally higher in our catalog than in the NCEDC catalog, and the rates vary independently between the catalogs. Interestingly, our approach detects many events

before the onset of elevated VTs in 10/2012 and elevated LPs in 11/2012 as seen in the NCEDC catalog. Figure 7c shows that tens of tremor signals and "unknown" events occur per week throughout the study period, while few "surface wave" events occurred at any time. In contrast, "sweep" events peak in August of 2012 and 2013, potentially reflecting increased air traffic for summer tourism.

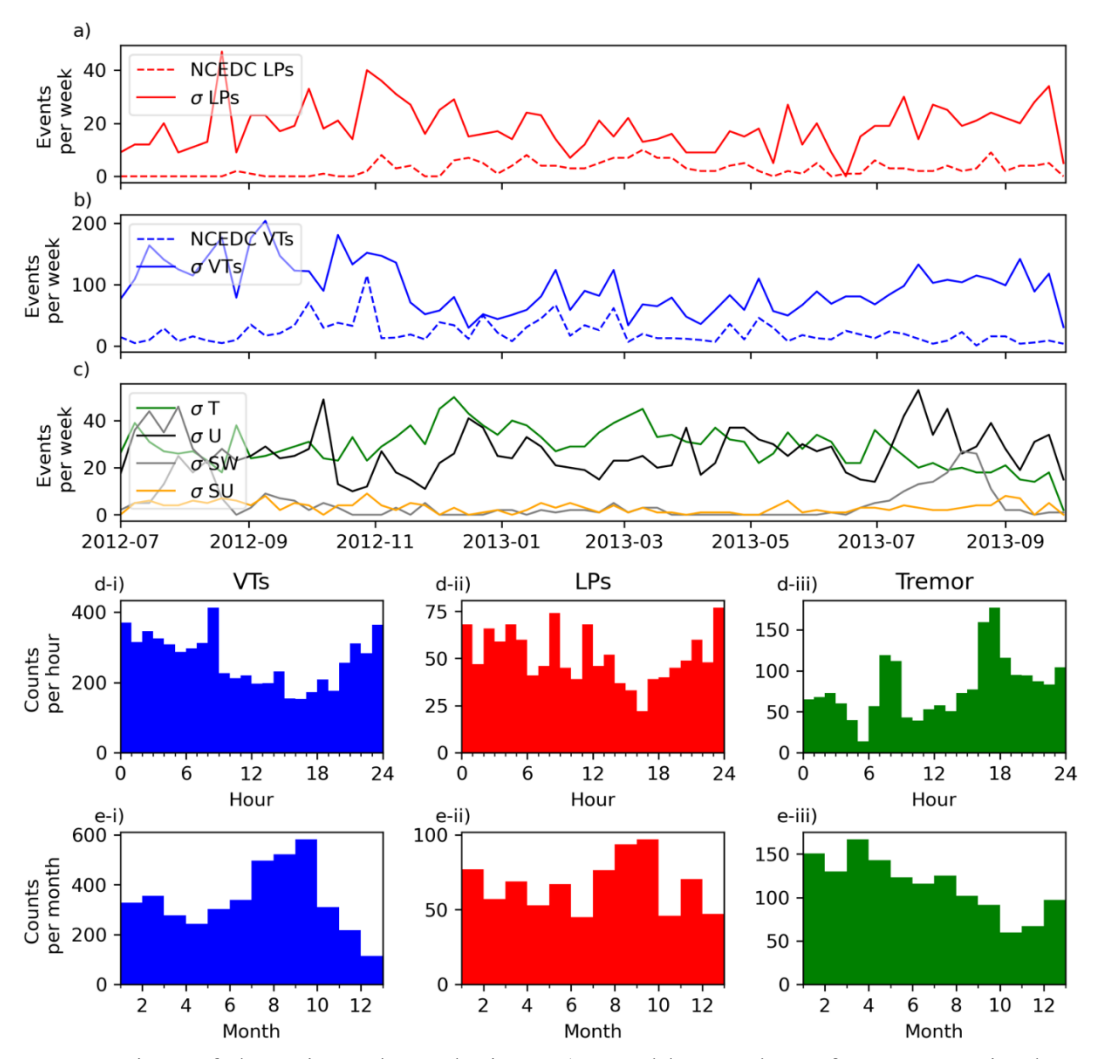


Figure 7. Overview of detections through time. a) Weekly number of LP events in the spectral width catalog (solid line) and the NCEDC catalog (dashed line). b) Weekly number of VT events in the spectral width catalog (solid line) and the NCEDC catalog (dashed line). c) Weekly number of other event types in the spectral width catalog including tremor (T, green), unknown (U, black), sweep (SW, gray) and surface waves (SU, orange). Histograms of the number of events per hour of the day (PST) are shown for VTs (d-i), LPs (d-ii) and tremor (d-iii). Histograms of the average number of events per month of the year are shown for VTs (e-i), LPs (e-ii) and tremor (e-iii).

Analysis of the number of events per hour of day (Figure 7d) and per month of the year (Figure 7e) also reflects trends in detection performance. Counts for VTs and LPs are lower in the afternoon hours while tremor detections are higher in the early morning and late afternoon hours.

VT and LP detections increase in the summer months of July–September while tremor detections peak in the winter months of December–May. Visual inspection of spectral width matrices indicates that long-duration and broadband coherence occurs, especially in the summer months, between 15:00 and 22:00 UTC (8:00–15:00 local time) with an hour-long break around 19:00-20:00 UTC (12:00–13:00 local time) (Figure 8a). These features occur exclusively during weekdays, suggesting a cultural origin such as construction, roadwork, or ski lift maintenance operations. Many of our detections may therefore correspond to the lowest- $\sigma$  portions of this cultural activity.

Also visible in Figure 8 are examples of regularly occurring tremor signals which vary by season and time of day. During both summer and winter, there is a persistent band of tremor around 4.5 Hz that begins abruptly around 15:00 UTC and ends abruptly around 2:00 UTC, corresponding roughly to local daytime hours. In summer there is often tremor during nighttime hours (2:00–15:00 UTC) with one or more bands between 5 and 7 Hz. We also observe this nighttime signal in winter, but the signal is weaker and occurs less often. The regular occurrence and abrupt transitions in the various tremor bands suggest cultural sources possibly related to chair lifts, water pumps, or geothermal power plant operations.

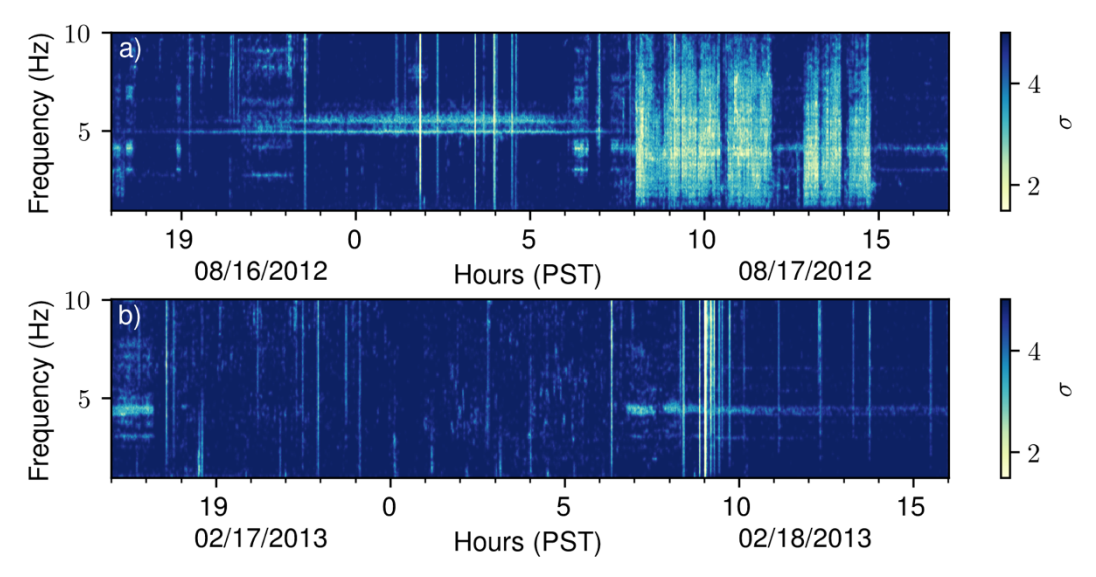


Figure 8. Examples of noise-reduced spectral width matrices for representative days in summer (a) and winter (b).

Although a full analysis of the new catalog is outside the scope of this study, examples of new LP and VT detections are shown in Figure 9. Typical LP waveforms (Figure 9a) lack clear phase arrivals while VT waveforms commonly feature distinct P- and S-wave arrivals (Figure 9b). The 50 highest-quality (high  $Q_d$ ) LP signals as recorded at station MINS (Figure 9c) show enrichment in spectral power between 1 and 4 Hz while the 50 highest-quality VTs are depleted in this frequency band (Figure 9d). Conversely, the VTs on average have higher power in the band 4–10 Hz relative to the LPs. Future work could investigate template matching or clustering to identify patterns in these new detections, and moment tensor (Dawson & Chouet, 2019) or focal mechanism inversions could be estimated to clarify their physical source mechanisms.

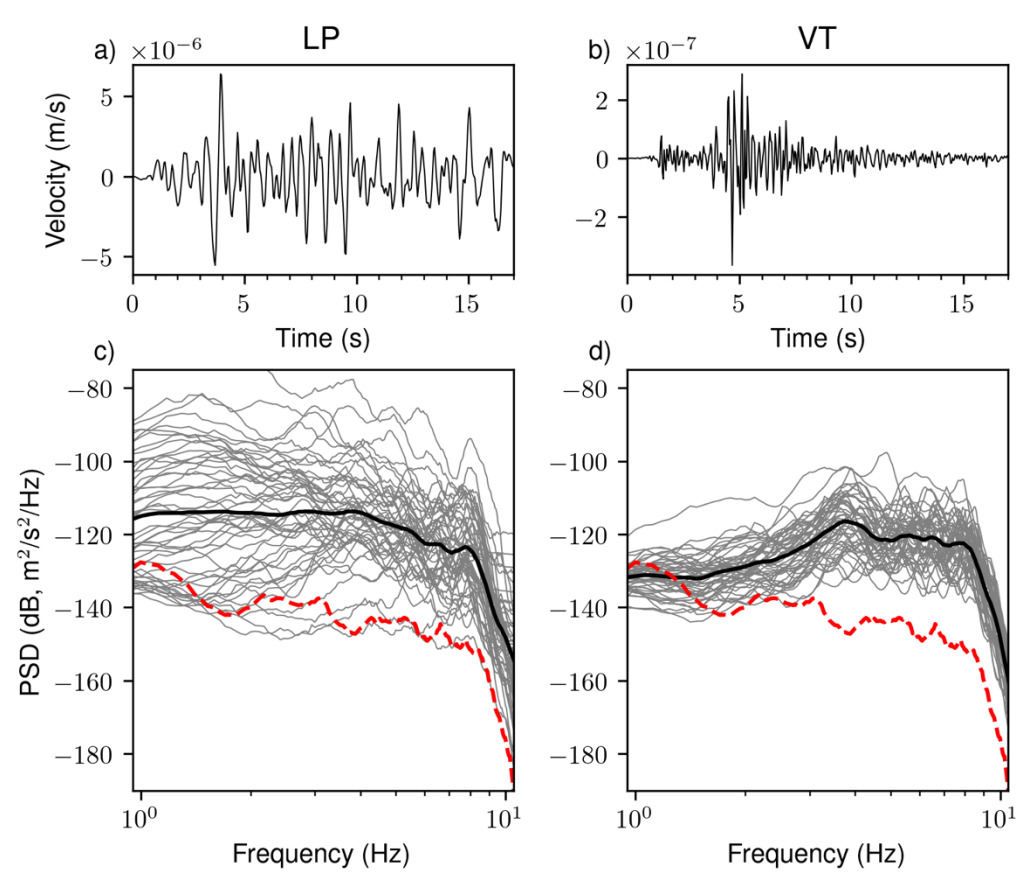


Figure 9. Examples of LP and VT detections in the new catalog. A) Vertical component velocity waveform (bandpass filtered 0.9-11 Hz) at station MINS for a LP detection at 19:51:58 PST on 05/23/2013. B) Vertical component velocity waveform (bandpass filtered 0.9-11 Hz) at station MINS a VT detection at 19:25:49 PST on 08/03/2012. C) Power spectral density (PSD) curves for the 17-second records of 50 highest-quality LP detections as recorded at station MINS. Gray lines show individual event spectra and black line shows the average. Dashed red line shows the result for a window of ambient noise 23:55:00 PST on 06/20/2013. D) PSD curves for the 50 highest-quality VT detections according to the same processing.

# **Initial Source Location Estimates**

The main contribution of this study is the detection workflow; however, a robust volcano-seismic monitoring system should also include source location estimates. We take a first step toward automated hypocenter estimation by implementing amplitude source locations (ASL) based on previous studies (e.g., Battaglia & Aki, 2003; Morioka et al., 2017). These locations provide an initial estimate that may be later refined by picking phases and using an arrival-time algorithm, or by implementing cross-correlation relative relocation.

Our location method is described in the Supplementary Materials, and our location results are summarized in Figure 10. Locations in the NCEDC catalog have well-defined planes of deep LPs (~10–15 km BSL) and separate clusters of shallow VTs (< 5 km BSL) and deep VTs (~15–20 km BSL), while ASL locations have diffuse clouds of LPs and VTs, with most events occurring near the surface. We note that direct comparison of locations for only the shared events between the catalogs indicates a general agreement between the two methods (Figure S8), although ASL

results are more scattered in depth. The shallow depths of the new events can therefore be considered a real feature, while additional investigation is required to determine the origin of the shallow signals.

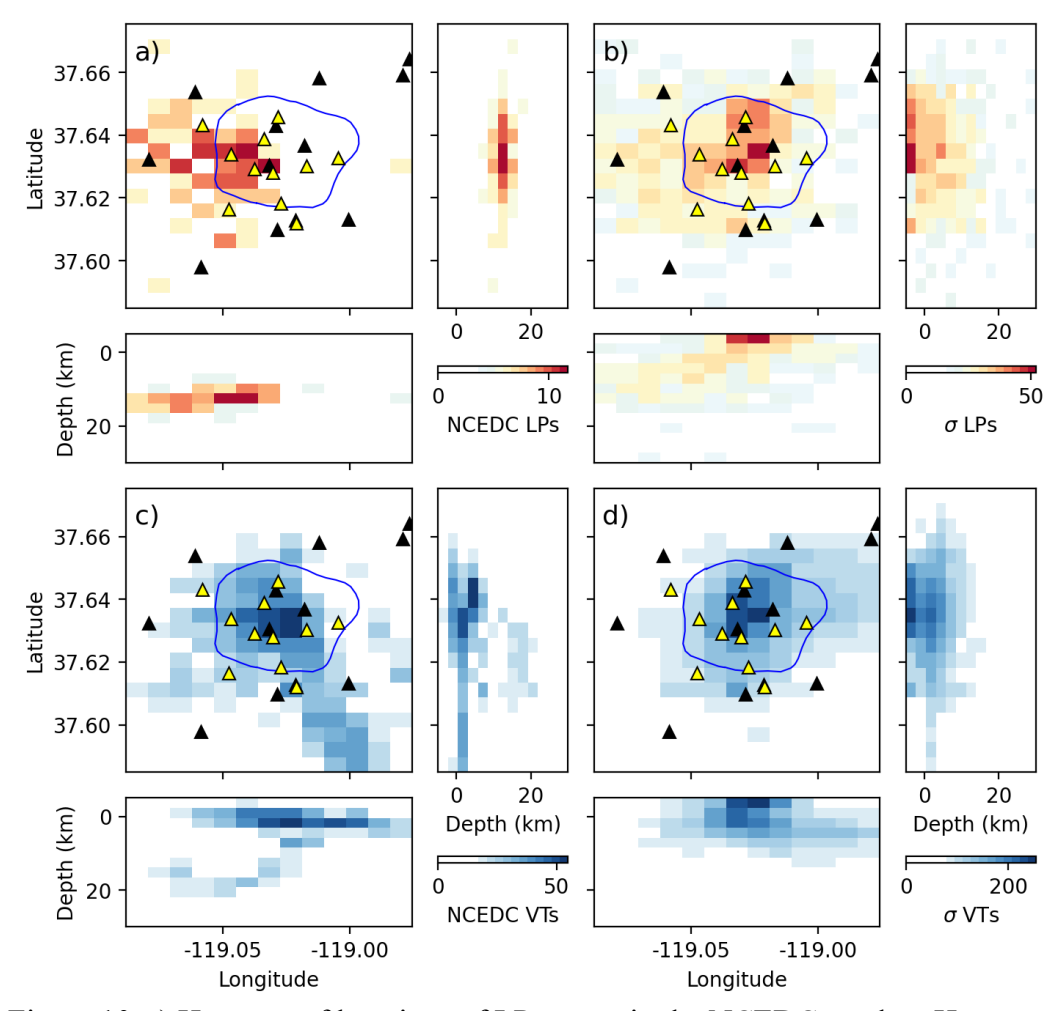


Figure 10. a) Heatmap of locations of LP events in the NCEDC catalog. Hypocenters are counted in lateral bins of 0.5 km and vertical bins of 2.5 km. Triangles represent seismic stations and blue line outlines the edifice as per

Figure 1. Location results are shown in the epicentral plane (center), depth-latitude plane (right, 7.6x vertical exaggeration) and longitude-depth plane (bottom, 7.6x vertical exaggeration). The map area is the same as

Figure 1b. b) Heatmap of amplitude source locations for LPs in the spectral width catalog. C) Heatmap of VT locations in the NCEDC catalog. D) Heatmap of VT locations in the spectral width catalog.

We also attempted to locate the continuous, narrowband tremor-like detections between 4.5 and 7 Hz (e.g., Figure 8) using a cross-correlation approach based on the network covariance

method (Soubestre et al., 2021; Journeau et al., 2022; Maher et al., 2023), but the results were strongly scattered in space and did not seem physical. We speculate that the signal-to-noise ratios of these signals are too low to retrieve stable locations (e.g., Maher et al., 2023). Since the signals are most likely cultural in origin, we did not attempt to locate them further with the amplitude method. We did not attempt to locate the LP or VT signals with the network covariance cross-correlation method because their durations are short relative to the covariance windows, such that a significant amount of background noise would affect the results.

#### **Discussion**

We introduce a practical workflow for automated detection of volcanic seismicity that adds new functionality to the network covariance method described by Seydoux et al. (2016). Our contributions suppress artifacts arising from zero-filled data gaps, boost signal-to-noise ratios in the spectral width matrix, enable independent detection of overlapping continuous and impulsive signals, and improve the time resolution of individual detections. Application of the workflow to data from Mammoth Mountain, California, reveals 1110 previously undetected LP events and 4702 new VT events as well as thousands of narrow-band, long-duration signals resembling tremor. Here we discuss some limitations of the method and directions for future work.

Although the method detects thousands of new events, the detection rate of known events in the NCEDC catalog is moderate for LPs (62%), and quite good for VTs (94%) compared to the > 90% accuracy rates achieved by supervised machine learning models (e.g., Lara-Cueva et al., 2016; Ruano et al., 2014). These models learn to recognize patterns, ensuring that signals with similar features to the training dataset will be detected. In contrast, the performance of the network covariance method is independent of patterns and relies on the degree of wavefield coherence between stations, the effectiveness of pre-processing steps in suppressing artifacts and background variations, and the thresholds used to separate noise from signal. Furthermore, the NCEDC catalog incorporates manual data review by analysts and includes events with low signal-to-noise ratios or separate entries for bursts of closely spaced events during swarms. Inspection of  $\sigma$  matrices for "false negatives" suggests that some missed events occur during time periods of diffuse broadband coherence during daylight hours (e.g., Figure 6a). These bursts probably represent cultural noise and may be less problematic in more remote study areas. Many other false negatives are visible as faint stripes in the  $\sigma$  matrices but are simply too weak to pass the threshold we set (e.g., Figure 6a, 6c). Reducing the threshold may detect additional events at the expense of more false positives (e.g., portions of the summer daytime bursts) and longer computation times for time refinement and location.

Another discrepancy between our results and the NCEDC catalog is in the locations (Figure 10). Our locations depend on the waveform amplitude measurements, homogeneous velocity model and quality factor assumption, and coda amplitude correction factors (Battaglia & Aki, 2003), while the NCEDC catalogs depend on the phase arrival pick times, 1D gradient velocity model, and travel-time residual correction factors (Klein, 2002). Amplitude-based locations are inherently less precise than pick-based locations and thus differences should be expected (Walsh et al., 2017, 2020). Despite these differences, our results are qualitatively comparable to the locations of events in the NCEDC catalog (Figure S7), yet many of the new events in our catalog have shallow locations on the edifice of Mammoth Mountain. Many of our detections are probably low-magnitude shallow events that were either missed by the current monitoring algorithm or detected but discarded due to poor location accuracy. Further analysis of these events and refinement of their locations could potentially yield new insights into shallow movement of

hydrothermal fluids or help to delineate the locations of small local faults. Nonetheless, even a rough location and depth estimate is crucial in interpretation. As our main focus here is the detection problem, we consider our locations strictly preliminary and leave detailed analysis of physical mechanisms to future work.

A limitation of the network covariance technique is the poor time resolution of short-duration detections, which arises from the need to average together many windowed cross-spectral estimates to obtain a non-degenerate eigenvalue decomposition. We initially attempted to solve this problem by using wavelet transforms in the formulation of the covariance matrix but were unable to obtain a stable eigenvalue decomposition even when averaging multiple samples. We attribute this to the instantaneous nature of the wavelet transform, which returns the precise phase of the wavelet at each point in time, combined with the lack of precise phase alignment between stations. Our proposed solution with the summed covariance matrix refines detection times by an order of magnitude relative to the initial detection window length and allows for detection of multiple events in a single  $\sigma$  window. This comes at the expense of additional computation and storage of matrices. Future work could explore alternative spectral transforms or time-refinement approaches to improve efficiency.

## **Conclusions**

Our proposed workflow is generally successful at recovering known events at Mammoth Mountain (62% of LPs and 94% of VTs in the NCEDC catalog) and reveals thousands of new events including LPs, VTs, and previously undetected tremor-like signals associated with cultural noise. This fully automatic workflow can be easily implemented for seismic monitoring in real time, enhancing the analyst-reviewed catalog and providing a more complete basis for research into physical source mechanisms. Future work could be directed toward implementing more accurate location estimates, automating the choices of user-defined parameters, and testing the method with additional datasets.

#### **Data and Resources**

We accessed waveform data and metadata for permanent stations (network codes NC and NN) through the Northern California Earthquake Data Center (doi:10.7932/NCEDC, last accessed 04/2024). We accessed waveform data and metadata for temporary stations (network code 8E) through the Incorporated Research Institutions for Seismology Data Management Center (<a href="http://ds.iris.edu/mda/8E">http://ds.iris.edu/mda/8E</a>, last accessed 04/2024). We used the covseisnet software package <a href="https://github.com/covseisnet/covseisnet">https://github.com/covseisnet/covseisnet</a> for covariance matrix estimation. Image processing operations were performed using functions from OpenCV (<a href="https://opencv.org">https://opencv.org</a>) and SciPy at (<a href="https://scipy.org">https://scipy.org</a>). Seismic data were handled using ObsPy (<a href="https://docs.obspy.org/">https://docs.obspy.org/</a>). Codes for the workflow described in this work are available at: <a href="https://doi.org/10.5066/P1PEHVRK">https://doi.org/10.5066/P1PEHVRK</a> (Maher et al., 2024). Supplemental material for this paper is available online and consists of supporting figures and a description of the location method. This work was partially supported by NSF grant EAR-1620576.

# **Declaration of Competing Interests**

The authors acknowledge that there are no conflicts of interest recorded.

# **Acknowledgments**

The authors thank Margaret Glasgow, Corentin Caudron, and an anonymous reviewer for their thoughtful comments that strengthened this manuscript. Any use of trade, firm, or product names is for descriptive purposes only and does not imply endorsement by the U.S. Government.

#### References

- Battaglia, J., & Aki, K. (2003). Location of seismic events and eruptive fissures on the Piton de la Fournaise volcano using seismic amplitudes. *Journal of Geophysical Research*, 108(B8), 1–14. https://doi.org/10.1029/2002jb002193
- Beyreuther, M., Carniel, R., & Wassermann, J. (2008). Continuous Hidden Markov Models: Application to automatic earthquake detection and classification at Las Canãdas caldera, Tenerife. *Journal of Volcanology and Geothermal Research*, *176*(4), 513–518. <a href="https://doi.org/10.1016/j.jvolgeores.2008.04.021">https://doi.org/10.1016/j.jvolgeores.2008.04.021</a>
- Bueno, A., Benitez, C., De Angelis, S., Diaz Moreno, A., & Ibanez, J. M. (2020). Volcano-Seismic Transfer Learning and Uncertainty Quantification with Bayesian Neural Networks. *IEEE Transactions on Geoscience and Remote Sensing*, 58(2), 892–902. <a href="https://doi.org/10.1109/TGRS.2019.2941494">https://doi.org/10.1109/TGRS.2019.2941494</a>
- Buurman, H., & West, M. E. (2010). Seismic precursors to volcanic explosions during the 2006 eruption of Augustine Volcano. *U.S. Geological Survey Professional Paper*, 1769, 41–57. <a href="https://doi.org/10.3133/pp17692">https://doi.org/10.3133/pp17692</a>
- Chouet, B. A. (1996). Long-period volcano seismicity: its source and use in eruption forecasting. *Nature*, *380*, 309–316. <a href="https://doi.org/10.1038/380309a0">https://doi.org/10.1038/380309a0</a>
- Chouet, B. A., & Matoza, R. S. (2013). A multi-decadal view of seismic methods for detecting precursors of magma movement and eruption. *Journal of Volcanology and Geothermal Research*, 252(July 2015), 108–175. <a href="https://doi.org/10.1016/j.jvolgeores.2012.11.013">https://doi.org/10.1016/j.jvolgeores.2012.11.013</a>
- Ciaramella, A., De Lauro, E., Falanga, M., & Petrosino, S. (2011). Automatic detection of long-period events at Campi Flegrei Caldera (Italy). *Geophysical Research Letters*, 38(18), 1–5. https://doi.org/10.1029/2011GL049065
- Cortés, G., Carniel, R., Lesage, P., Mendoza, M. Á., & Della Lucia, I. (2021). Practical Volcano-Independent Recognition of Seismic Events: VULCAN.ears Project. *Frontiers in Earth Science*, 8(January), 1–11. <a href="https://doi.org/10.3389/feart.2020.616676">https://doi.org/10.3389/feart.2020.616676</a>
- Dawson, P., & Chouet, B. (2019). Long Period Seismicity at Mammoth Mountain, California. *Journal of Geophysical Research: Solid Earth*, 124(7), 6751–6778. https://doi.org/10.1029/2019JB017580
- Dawson, P., Chouet, B., & Pitt, A. (2016). Tomographic image of a seismically active volcano: Mammoth Mountain, California. *Journal of Geophysical Research: Solid Earth*, 121, 114–133. <a href="https://doi.org/10.1002/2015JB012537">https://doi.org/10.1002/2015JB012537</a>
- Dey, S. (2018). Hands-On Image Processing with Python. In *Packt Publishing Ltd*. <u>GitHub-PacktPublishing/Hands-On-Image-Processing-with-Python</u>
- Galluzzo, D., Nardone, L., La Rocca, M., Esposito, A. M., Manzo, R., & Di Maio, R. (2020). Statistical moments of power spectrum: A fast tool for the classification of seismic events recorded on volcanoes. *Advances in Geosciences*, *52*, 67–74. <a href="https://doi.org/10.5194/adgeo-52-67-2020">https://doi.org/10.5194/adgeo-52-67-2020</a>

- Hildreth, W., & Fierstein, J. (2016). Eruptive history of Mammoth Mountain and its mafic periphery, California. *U.S. Geological Survey Professional Paper 1812*. https://doi.org/10.3133/pp1812
- Hill, D. P., Ellsworth, W. L., Johnston, M. J. S., Langbein, J. O., Oppenheimer, D. H., Pitt, A. M., Reasenberg, P. A., Sorey, M. L., & McNutt, S. R. (1990). The 1989 Earthquake Swarm beneath Mammoth Mountain, California: an initial look at the 5 May through 30 September Activity. *Bulletin of the Seismological Society of America*, 80(2), 325–339. <a href="https://doi.org/10.1785/BSSA0800020325">https://doi.org/10.1785/BSSA0800020325</a>
- Hill, D. P., & Prejean, S. (2005). Magmatic unrest beneath Mammoth Mountain, California. *Journal of Volcanology and Geothermal Research*, *146*(4), 257–283. https://doi.org/10.1016/j.jvolgeores.2005.03.002
- Hotovec-Ellis, A. J., Shelly, D. R., Hill, D. P., Pitt, A. M., Dawson, P. B., & Chouet, B. A. (2018). Deep fluid pathways beneath Mammoth Mountain, California, illuminated by migrating earthquake swarms. *Science Advances*, *4*(8), eaat5258. <a href="https://doi.org/10.1126/sciadv.aat5258">https://doi.org/10.1126/sciadv.aat5258</a>
- Journeau, C., Shapiro, N. M., Seydoux, L., Soubestre, J., Ferrazzini, V., & Peltier, A. (2020). Detection, Classification, and Location of Seismovolcanic Signals with Multicomponent Seismic Data: Example from the Piton de la Fournaise Volcano (La Réunion, France). *Journal of Geophysical Research: Solid Earth*, 125(8), 1–19. <a href="https://doi.org/10.1029/2019JB019333">https://doi.org/10.1029/2019JB019333</a>
- Journeau, C., Shapiro, N. M., Seydoux, L., Soubestre, J., Koulakov, I. Y., Jakovlev, A. V., Abkadyrov, I., Gordeev, E. I., Chebrov, D. V., Droznin, D. V., Sens-Schönfelder, C., Luehr, B. G., Tong, F., Farge, G., & Jaupart, C. (2022). Seismic tremor reveals active trans-crustal magmatic system beneath Kamchatka volcanoes. *Science Advances*, 8(5), 1–10. https://doi.org/10.1126/sciadv.abj1571
- Klein, Fred. W. (2002). User's Guide to HYPOINVERSE-2000, a Fortran Program to Solve for Earthquake Locations and Magnitudes. *U.S. Geological Survey Open File Report 02-171*, 123 pp. <a href="https://doi.org/10.3133/ofr02171">https://doi.org/10.3133/ofr02171</a>
- Langet, N., Maggi, A., Michelini, A., & Brenguier, F. (2014). Continuous kurtosis-based migration for seismic event detection and location, with application to Piton de la Fournaise volcano, La Réunion. *Bulletin of the Seismological Society of America*, 104(1), 229–246. https://doi.org/10.1785/0120130107
- Lara-Cueva, R. A., Benítez, D. S., Carrera, E. V., Ruiz, M., & Rojo-Álvarez, J. L. (2016). Feature selection of seismic waveforms for long period event detection at Cotopaxi Volcano. *Journal of Volcanology and Geothermal Research*, *316*, 34–49. https://doi.org/10.1016/j.jvolgeores.2016.02.022
- Lewicki, J. L., Evans, W. C., Montgomery-Brown, E. K., Mangan, M. T., King, J. C., & Hunt, A. G. (2019). Rate of Magma Supply Beneath Mammoth Mountain, California, Based on Helium Isotopes and CO2 Emissions. *Geophysical Research Letters*, 46(9), 4636–4644. https://doi.org/10.1029/2019GL082487
- Lewicki, J. L., Hilley, G. E., Shelly, D. R., King, J. C., McGeehin, J. P., Mangan, M., & Evans, W. C. (2014). Crustal migration of CO2-rich magmatic fluids recorded by tree-ring radiocarbon and seismicity at Mammoth Mountain, CA, USA. *Earth and Planetary Science Letters*, 390, 52–58. <a href="https://doi.org/10.1016/j.epsl.2013.12.035">https://doi.org/10.1016/j.epsl.2013.12.035</a>
- Lin, G. (2013). Seismic investigation of magmatic unrest beneath Mammoth Mountain, California, USA. *Geology*, 41(8), 847–850. <a href="https://doi.org/10.1130/G34062.1">https://doi.org/10.1130/G34062.1</a>

- Maher, S. P., Dawson, P., Hotovec-Ellis, A., Thelen, W. A., Jolly, A., Bennington, N., Chang, J. C., & Dotray, P. (2023). Characterizing and Locating Seismic Tremor during the 2022 Eruption of Mauna Loa Volcano, Hawai'i, with Network Covariance. *The Seismic Record*, 3(3), 228–238. https://doi.org/10.1785/0320230020
- Maher, S. P., Dawson, P. D., Hotovec-Ellis, A. J., and Thelen, W. A. (2024) covdetect network covariance event detector (Version 0.0.0), *U.S. Geological Survey Software Release*. https://doi.org/10.5066/P1PEHVRK.
- Malfante, M., Dalla Mura, M., Metaxian, J. P., Mars, J. I., Macedo, O., & Inza, A. (2018). Machine Learning for Volcano-Seismic Signals: Challenges and Perspectives. *IEEE Signal Processing Magazine*, 35(2), 20–30. https://doi.org/10.1109/MSP.2017.2779166
- Matoza, R. S., Shearer, P. M., & Okubo, P. G. (2014). High-precision relocation of long-period events beneath the summit region of Kīlauea Volcano, Hawai'i, from 1986 to 2009. *Geophysical Research Letters*, 41(10), 3413–3421. https://doi.org/10.1002/2014GL059819
- McNutt, S. R. (1996). Seismic Monitoring and Eruption Forecasting of Volcanoes: A Review of the State-of-the-Art and Case Histories. In *Monitoring and Mitigation of Volcano Hazards* (p. 842). <a href="https://doi.org/10.1007/978-3-642-80087-0">https://doi.org/10.1007/978-3-642-80087-0</a>
- McNutt, S. R., Thompson, G., Johnson, J., Angelis, S. De, & Fee, D. (2015). Seismic and Infrasonic Monitoring. In *The Encyclopedia of Volcanoes* (pp. 1071–1099). Elsevier Inc. https://doi.org/10.1016/b978-0-12-385938-9.00063-8
- Messina, A., & Langer, H. (2011). Pattern recognition of volcanic tremor data on Mt. Etna (Italy) with KKAnalysis-A software program for unsupervised classification. *Computers and Geosciences*, 37(7), 953–961. <a href="https://doi.org/10.1016/j.cageo.2011.03.015">https://doi.org/10.1016/j.cageo.2011.03.015</a>
- Morioka, H., Kumagai, H., & Maeda, T. (2017). Theoretical basis of the amplitude source location method for volcano-seismic signals. *Journal of Geophysical Research: Solid Earth*, 122(8), 6538–6551. https://doi.org/10.1002/2017JB013997
- Peiffer, L., Wanner, C., & Lewicki, J. L. (2018). Unraveling the dynamics of magmatic CO2 degassing at Mammoth Mountain, California. *Earth and Planetary Science Letters*, 484, 318–328. <a href="https://doi.org/10.1016/j.epsl.2017.12.038">https://doi.org/10.1016/j.epsl.2017.12.038</a>
- Permana, T., Nishimura, T., Nakahara, H., & Shapiro, N. (2022). Classification of volcanic tremors and earthquakes based on seismic correlation: application at Sakurajima volcano, Japan. *Geophysical Journal International*, 229(2), 1077–1097. https://doi.org/10.1093/gji/ggab517
- Pitt, A. M., & Hill, D. P. (1994). Long-period earthquakes in the Long Valley Caldera Region, eastern California. *Geophysical Research Letters*, 21(16), 1679–1682. https://doi.org/10.1029/94GL01371
- Pitt, A. M., Hill, D. P., Walter, S. W., & Johnson, M. J. S. (2002). Midcrustal, Long-period Earthquakes beneath Northern California Volcanic Areas. *Seismological Research Letters*, 73(2), 144–152. https://doi.org/10.1785/gssrl.73.2.144
- Prejean, S., Stork, A., Ellsworth, W., Hill, D., & Julian, B. (2003). High precision earthquake locations reveal seismogenic structure beneath Mammoth Mountain, California. *Geophysical Research Letters*, 30(24), 4–7. <a href="https://doi.org/10.1029/2003GL018334">https://doi.org/10.1029/2003GL018334</a>
- Reynen, A., & Audet, P. (2017). Supervised machine learning on a network scale: Application to seismic event classification and detection. *Geophysical Journal International*, 210(3), 1394–1409. https://doi.org/10.1093/gji/ggx238

- Ruano, A. E., Madureira, G., Barros, O., Khosravani, H. R., Ruano, M. G., & Ferreira, P. M. (2014). Seismic detection using support vector machines. *Neurocomputing*, *135*, 273–283. https://doi.org/10.1016/j.neucom.2013.12.020
- Sainburg, T., Thielk, M., & Gentner, T. Q. (2020). Finding, visualizing, and quantifying latent structure across diverse animal vocal repertoires. In *PLoS Computational Biology* (Vol. 16, Issue 10). <a href="https://doi.org/10.1371/journal.pcbi.1008228">https://doi.org/10.1371/journal.pcbi.1008228</a>
- Seydoux, L., Balestriero, R., Poli, P., Hoop, M. de, Campillo, M., & Baraniuk, R. (2020). Clustering earthquake signals and background noises in continuous seismic data with unsupervised deep learning. *Nature Communications*, *11*(1). https://doi.org/10.1038/s41467-020-17841-x
- Seydoux, L., Shapiro, N. M., De Rosny, J., Brenguier, F., & Landès, M. (2016). Detecting seismic activity with a covariance matrix analysis of data recorded on seismic arrays. *Geophysical Journal International*, 204(3), 1430–1442. https://doi.org/10.1093/gji/ggv531
- Shapiro, N. M., Soubestre, J., Journeau, C. (2023). Network-based analysis of seismo-volcanic tremors. *IAVCEI Book Modern Volcano Monitoring*. <a href="https://cnrs.hal.science/ISTERRE/insu-04167423v1">https://cnrs.hal.science/ISTERRE/insu-04167423v1</a>
- Shelly, D. R., & Hill, D. P. (2011). Migrating swarms of brittle-failure earthquakes in the lower crust beneath Mammoth Mountain, California. *Geophysical Research Letters*, 38(20), 1–6. https://doi.org/10.1029/2011GL049336
- Shelly, D. R., Taira, T., Prejean, S. G., Hill, D. P., & Dreger, D. S. (2015). Fluid-faulting interactions: Fracture-mesh and fault-valve behavior in the February 2014 Mammoth Mountain, California, earthquake swarm. *Geophysical Research Letters*, 42(14), 5803–5812. <a href="https://doi.org/10.1002/2015GL064325">https://doi.org/10.1002/2015GL064325</a>
- Sorey, M. L., Evans, W. C., Kennedy, B. M., Farrar, C. D., Hainsworth, L. J., & Hausback, B. (1998). Carbon dioxide and helium emissions from a reservoir of magmatic gas beneath Mammoth Mountain, California. *Journal of Geophysical Research*, 103(B7), 15303–15323. <a href="https://doi.org/10.1029/98JB01389">https://doi.org/10.1029/98JB01389</a>
- Soubestre, J., Chouet, B., & Dawson, P. (2021). Sources of Volcanic Tremor Associated With the Summit Caldera Collapse During the 2018 East Rift Eruption of Kīlauea Volcano, Hawai'i. *Journal of Geophysical Research: Solid Earth*, *126*(6), 1–33. <a href="https://doi.org/10.1029/2020jb021572">https://doi.org/10.1029/2020jb021572</a>
- Soubestre, J., Seydoux, L., Shapiro, N. M., de Rosny, J., Droznin, D. V., Droznina, S. Y., Senyukov, S. L., & Gordeev, E. I. (2019). Depth Migration of Seismovolcanic Tremor Sources Below the Klyuchevskoy Volcanic Group (Kamchatka) Determined From a Network-Based Analysis. *Geophysical Research Letters*, 46(14), 8018–8030. <a href="https://doi.org/10.1029/2019GL083465">https://doi.org/10.1029/2019GL083465</a>
- Soubestre, J., Shapiro, N. M., Seydoux, L., de Rosny, J., Droznin, D. V., Droznina, S. Y., Senyukov, S. L., & Gordeev, E. I. (2018). Network-Based Detection and Classification of Seismovolcanic Tremors: Example From the Klyuchevskoy Volcanic Group in Kamchatka. *Journal of Geophysical Research: Solid Earth*, 123(1), 564–582. <a href="https://doi.org/10.1002/2017JB014726">https://doi.org/10.1002/2017JB014726</a>
- Thompson, G. (2015). Seismic Monitoring of Volcanoes. In *Encyclopedia of Earthquake Engineering*. Springer-Verlag. https://doi.org/10.1007/978-3-642-36197-5 41-1
- Titos, M., Bueno, A., García, L., Benítez, C., & Segura, J. C. (2020). Classification of Isolated Volcano-Seismic Events Based on Inductive Transfer Learning. *IEEE Geoscience and Remote Sensing Letters*, 17(5), 869–873. <a href="https://doi.org/10.1109/LGRS.2019.2931063">https://doi.org/10.1109/LGRS.2019.2931063</a>

- Titos, M., Bueno, A., García, L., Benítez, M. C., & Ibañez, J. (2019). Detection and Classification of Continuous Volcano-Seismic Signals with Recurrent Neural Networks. *IEEE Transactions on Geoscience and Remote Sensing*, *57*(4), 1936–1948. <a href="https://doi.org/10.1109/TGRS.2018.2870202">https://doi.org/10.1109/TGRS.2018.2870202</a>
- Tozer, B., Sandwell, D. T., Smith, W. H.F., Olson, C., Beale, J. R., Wessel, P. (2019). Global Bathymetry and Topography at 15 Arc Sec: SRTM15+. *Earth and Space Science*, 6(10), 1847-1864. <a href="https://doi.org/10.1029/2019EA000658">https://doi.org/10.1029/2019EA000658</a>
- Walsh, B., Jolly, A. D., & Procter, J. (2017). Calibrating the amplitude source location (ASL) method by using active seismic sources: An example from Te Maari volcano, Tongariro National Park, New Zealand. *Geophysical Research Letters*, 44(8), 3591–3599. https://doi.org/10.1002/2017GL073000
- Walsh, B., Procter, J., & Jolly, A. (2020). Improving the amplitude source location (ASL) method using multicomponent seismic data: An assessment with active source seismic data. *Bulletin of the Seismological Society of America*, *110*(1), 250–269. https://doi.org/10.1785/0120190063
- Yoon, C. E., O'Reilly, O., Bergen, K. J., & Beroza, G. C. (2015). Earthquake detection through computationally efficient similarity search. *Science Advances*, *I*(11). https://doi.org/10.1126/sciadv.1501057